Detection Limit of Defect-Induced Strain in GaN Evaluated by Valence EELS and Correlated Structural Analysis

Shunsuke Yamashita[1*], Jun Kikkawa[2], Susumu Kusanagi[1], Ichiro Nomachi[1], Ryoji Arai[1], Yuya Kanitani[1], Koji Kimoto[2], and Yoshihiro Kudo[1]

[1] Research Division 3, Sony Semiconductor Solutions Corporation, 4-14-1 Asahi-cho, Atsugi, Kanagawa, 243-0014 Japan

[2] Center for Basic Research on Materials, National Institute for Materials Science, 1-1 Namiki, Tsukuba, 305-0044 Japan

[*] Correspondence should be addressed to Shunsuke Yamashita

Phone: +81-70-7598-7860

E-mail: Shunsuke.A.Yamashita@sony.com

Running title: Detection limit of defect-induced strain by VEELS

Keywords: Limit of detection, Detection threshold, Physical analysis, Gallium nitride, Valence electron energy loss spectroscopy (VEELS), Low-loss spectrum

Total number of pages: 25

Total number of figures: 6

Abstract

Crystal defects are intrinsically linked to the electrical and optical properties of semiconductor materials, making their nanoscale detection essential across all phases (from research and development to manufacturing). Electron energy loss spectroscopy (EELS) in scanning transmission electron microscopy (STEM) has emerged as a promising technique for detecting even point defects due to the shape modulation in valence-loss spectra induced by defects. However, previous studies have primarily focused on qualitative detection, leaving the detection limit, *i.e.,* the minimum detectable concentration, insufficiently explored. To experimentally evaluate the detection limit of defects and clarify the application scope of valence EELS, we prepared GaN samples with controlled defect concentrations along the depth direction using multi-step He-ion implantation and acquired valence-loss spectra at each depth. Based on the simulated depth profile of defects, we evaluated the detection limit from the depth at which significant modulation in the spectral shape was observed. The detection limit fundamentally depends on the signal-to-noise ratio of the valence-loss spectra. Under typical STEM conditions with an electron dose of 5×10^5 $e^-/Å^2$, the detection limit of defects in GaN was determined to be 0.35% (3500 ppm). Detailed structural analysis revealed that GaN contains implantation-induced defects and their clusters, and exhibits lattice strain and local disorder while retaining its wurtzite structure. The shape modulation in the valence-loss spectra was attributed to the indirect detection of defects through the surrounding strain fields.

Introduction

The detection limit is a fundamental performance metric of physical analytical methods, alongside spatial resolution. Transmission electron microscopy (TEM) is a unique technique that offers both high spatial resolution and detection sensitivity. Over the decades, the direct observation and identification of individual atoms, molecules, and defects have been extensively explored [1–6], demonstrating that the minimum detectable mass in TEM can reach the single-atom or single-molecule level. Utilizing ultrathin TEM samples or low-dimensional materials has become a common strategy for single-atom detection because reducing the thickness of TEM samples effectively increases the ratio of a specific analyte to the base material when the analyte is present. Conversely, the detection limit can also be defined as the minimum detectable concentration [7]. Detecting low-concentration impurity atoms or defects is often a critical requirement in the semiconductor industry. However, for defects in three-dimensional structures, experimental data on the minimum detectable concentration remain scarce due to the absence of suitable nanoscale detection methods.

Electron energy loss spectroscopy (EELS) in scanning transmission electron microscopy (STEM) has demonstrated the capability to detect and identify defects through shape modulation in valence-loss spectra [8–11]. Our previous study revealed that crystal imperfections in Ga-ion implanted GaN induced mid-gap states, leading to intensity modulation in the valence-loss spectra that reflected the defect concentration [11]. Another study reported that different point defects, such as interstitials and vacancies, could be distinguished with a spatial resolution of approximately 10 nm in boron-incorporated AlN films, aided by density functional theory [9]. Although core-loss EELS, which has sensitivity to local atomic arrangements and better spatial resolution, also has the capability for defect detection, ionization edges in appearing high-energy

loss regions often suffer from lower signal intensities. Thus, valence EELS has emerged as a promising technique for detecting defects in three-dimensional structures at the nanoscale. However, previous studies have primarily focused on qualitative detection, leaving the minimum detectable concentration insufficiently explored.

The purpose of this study is to evaluate the detection limit of defects using valence EELS and to clarify its applicability for defect detection at the nanoscale. To achieve this, we prepared GaN with a controlled concentration of defects along the depth direction as a model system. In contrast to our previous study that involved various defective structures intentionally induced through high dose ion implantation [11], ion doses in this study were kept relatively low to retain the original crystal structure. Valence-loss spectra were acquired at each depth under high-energy resolution conditions enabled by a monochromatic electron source. The detection limit is defined as the threshold distinguishing desired signals from background noise. Thus, we examined the maximum depth at which the spectral shape significantly deviated from that observed at depths with sufficiently low defect concentrations. Subsequently, we determined the detection limit based on defect concentrations estimated through an ion implantation simulation. A detailed structural analysis was conducted to provide supporting evidence that the spectral shape modulation was induced by defects resulting from implantation.

Methods

Sample preparation

Multi-step He-ion implantation was performed to prepare GaN samples with a controlled concentration of defects along the depth direction. Figure 1(a) presents a schematic illustration of the three-step He-ion implantation process, in which ion doses of 10^{15}, 10^{13}, and 10^{11} atoms/cm^2

were used for implantation energies of 20, 130, and 350 keV, respectively. The implantation angle was set to 7° off from the GaN (0001) surface, and post-annealing was not performed. Figures 1(b) and 1(c) represent the resulting distributions of He-ions and defects simulated using the Stopping and Range of Ions in Matter (SRIM) software [12]. Figure 1(b) also includes the He-ion distribution measured by secondary ion mass spectroscopy (SIMS) represented by red filled markers. To detect low-concentration He-ions with high sensitivity, the laser ionization mass nanoscope (LIMAS) at Hokkaido University, which enables post-laser ionization, was utilized [13]. The He-ion distribution exhibits three peaks, and the second peak with a concentration lower than 10^{18} atoms/cm^2 was experimentally observed due to the high-sensitivity measurement. For the first peak, the depth and concentration showed good agreement between the experimental results and simulation. Consequently, we assumed that the concentration of defects near the surface as simulated by the SRIM is reliable and used this depth profile to evaluate the detection limit.

Fig. 1

To experimentally evaluate the detection limit, a sample containing at least one analyte in an analytical volume at a certain measurement point must be used. If the analytical volume contains only one analyte, the concentration corresponds to the lower limit of the evaluation and is defined as the physical detection limit (*i.e.*, the physical limit). The physical limit can be calculated as the inverse of the number of atoms constituting the analytical volume. For the detection limit evaluation, a TEM sample with a sufficiently low physical limit is indispensable. In STEM, the analytical volume corresponds to the interaction volume where the electron probe

interacts with the sample, which can be approximated by the product of the probe size (*i.e.*, the analytical area) and TEM sample thickness. Additionally, the delocalization effect of inelastic scattering must be considered for valence EELS measurements [14]. Coulomb interaction between an electron probe and electrons in a sample can occur over a range wider than the probe diameter. For example, valence electrons can be excited even by an electron probe slightly away from atoms. The degree of the interaction depends on the energy of the incident electrons and the energy loss range of interest. For energy losses around 3–5 eV near the interband transition of GaN, the delocalization factor is estimated to be 4 nm at an acceleration voltage of 30 kV. Thus, the analytical area was assumed to be 16 nm^2 in this study. Figure 1(d) illustrates the physical limit as a function of TEM sample thickness for GaN (atomic density: 88 atoms/nm^3). When the TEM sample thickness is 50 nm, the number of atoms within the analytical volume is approximately 70,400, and the physical limit is calculated to be 14 ppm. This value is sufficiently low and suitable for evaluating the detection limit. Thus, we prepared a TEM sample with a thickness of 50 ± 5 nm from the surface to a depth of 1600 nm using a focused ion beam (FIB) system (Helios400S, Thermo Fisher Scientific). The thickness was measured using the EELS log-ratio method [15]. The mean free paths of inelastic scattering in GaN were calculated to be 40 nm at 30 kV and 142 nm at 300 kV [16]. To eliminate ion-induced damage layers on the processed surface, low-acceleration Ar ion milling (Gentle Mill, Technoorg Linda) was performed at an acceleration voltage of 350 V.

STEM-EELS

We utilized an aberration-corrected and monochromated TEM (ThemisZ, Thermo Fisher Scientific). Valence-loss spectra were collected from the surface to a depth of 1600 nm in 10.2-

nm steps using a Gatan imaging filter system (GIF Quantum 970) and a charge-coupled device (CCD) camera (994 US1000XP U^+, Gatan). To enhance the signal-to-noise ratios (SNRs), 18 spectra were acquired at each depth and integrated. The acceleration voltage was set at 30 kV to minimize the effects of Cherenkov radiation [17]. The energy resolution, defined by the full width at half maximum of the zero-loss peak (ZLP), was 70 meV, with an energy dispersion of 5 meV/channel. The convergence angle of the focused electron probe and collection angle were set to 13.9 and 18.0 mrad, respectively. The probe current was set to 100 pA, with a dwell time of 0.5 s/pixel. The electron dose was calculated to be 3.1×10^8 e^-/pixel (= 3.0×10^4 $e^-/Å^2$).

Structural analysis

The atomic structures of He-ion implanted GaN were investigated using X-ray energy dispersive spectroscopy (XEDS), four-dimensional (4D)-STEM, and atomic resolution STEM imaging. For 4D-STEM, the same TEM used for the STEM-EELS measurements was employed at an acceleration voltage of 30 kV. The convergence angle of the focused electron probe was set to 7.5 mrad, with a probe current of 25 pA. The number of measurement points in real space was 272 × 37 pixels, while the size of each diffraction pattern was 256 × 256 pixels. The pixel size was set to 5 nm/pixel in real space and 1 mrad/pixel in reciprocal space. The dwell time was 0.1 s/pixel.

For XEDS elemental analysis and atomic-resolution STEM observation, an aberration-corrected TEM (JEM-ARM300F, JEOL) was used at an acceleration voltage of 300 kV. The convergence angle of the focused electron probe was set to 24 mrad. The Cliff-Lorimer method was used for quantitative analysis of the XEDS spectra and thus the effect of absorption was not considered. To interpret the XEDS elemental analysis results, electron propagation in the GaN

crystal was simulated using the abTEM Python package [18]. In STEM observation, high-angle annular dark-field (HAADF) images, which provide Z-contrast [19], and annular bright-field (ABF) images, which are capable of visualizing both Ga and N atomic columns [20], were acquired simultaneously. The detection angle range was 53–175 mrad for HAADF and 11–22 mrad for ABF. To enhance the SNR, STEM images were obtained by integrating 50 fast-scan images (dwell time: 2 μs/pixel), following drift correction [21].

Results and Discussion

Evaluation of the detection limit using valence-loss spectra

First, we evaluated the detection limit by analyzing shape modulation in the valence-loss spectra. Figures 2(a) and 2(b) show the annular dark-field (ADF) image indicating the region of the EEL spectrum imaging measurement and integrated spectra at each depth, respectively. To facilitate the interpretation of shape modulation in the valence-loss spectra, smoothed spectra from the surface to a depth of 600 nm are presented in Fig. 2(c). Interface plasmons do not affect the evaluation because their effect is limited to the extreme vicinity of the interface. In contrast to our previous study [11], no clear mid-gap states were observed due to the lower defect concentration. We specifically focused on the two most modulated regions of the spectra: the inflection points at the onset marked by a red arrow and the slopes in the 3.6–4.6 eV range indicated by red lines. Figures 2(d) and 2(e) illustrate the depth dependence of the inflection points and slopes at 3.6–4.6 eV, respectively. No significant changes were observed below a depth of 600 nm in either case; thus, this depth was defined as the background region where the defect concentration was sufficiently low. Each background region was then approximated using a linear function, and the standard deviation (σ) was measured using all data points below a

depth of 600 nm. The shaded areas in Fig. 2(d) and 2(e) represent three standard deviations (±3σ) from the approximated lines, encompassing 99.7% of the data under the assumption of a normal distribution. The obliquity from the surface to the deep region probably reflects the variation in the background intensity due to the slight difference in the TEM sample thickness; however, the effect on the spectral shape is not significant. From a depth of 200 nm to the surface, two significant changes beyond the 3σ region were observed: a shift of the inflection point to higher energy losses by approximately 50 meV and a decrease in the slope at 3.6–4.6 eV. According to Fig. 1(c), the defect concentration at a depth of 200 nm is estimated to be 3.1×10^{20} defects/cm^3. Therefore, the detection limit of defects in GaN (8.8×10^{22} atoms/cm^3) was evaluated to be 0.35% (3500 ppm). Note that the number of "defects" refers to the number of "vacancies" in the SRIM software. If interstitial atoms formed alongside vacancies are also considered as "defects," the detection limit would double to 0.70%.

Fig. 2

Electron-dose dependence of detection limits

In general, the detection limit is influenced by the measurement conditions, particularly the SNR of a spectrum. A lower SNR raises (worsens) the detection limit, whereas a higher SNR lowers (improves) it. Thus, understanding the relationship between the SNR of valence-loss spectra and the detection limit of defects is of practical importance. Among noise sources, we focused on shot noise, which depends on an electron dose. This is because shot noise is an inevitable major noise source in electron detection and is important in any detection system.

To investigate this relationship, we systematically reduced the number of integrated spectra at each depth to artificially vary the electron dose and examined the corresponding changes in the detection limit and SNR. Because the inflection points cannot be reliably determined without smoothing, we focused solely on the slope in the 3.6–4.6 eV range. Figure 3(a) illustrates the effect of the electron dose on the depth dependence of the slopes in the 3.6–4.6 eV range. The number of integrated spectra was systematically reduced from 18 as shown in Fig. 2(e) to 16, 9, 4, and then 1. The corresponding electron doses are indicated at the top of the figure. As the electron dose decreases, the SNR of the valence-loss spectra reduces, leading to an increase in the standard deviation of the slope. The increase in the standard deviation causes the maximum depth, indicated by the red arrows in Fig. 3(a), at which significant changes in the slope are observed to become shallower, ultimately resulting in a higher detection limit. The detection limits were determined using the maximum depth in Fig. 3(a) and the corresponding defect concentrations estimated from Fig. 1(c). Figure 3(b) presents the evaluated detection limit corresponding to each electron dose. These results indicate that the detection limit increases to approximately 2% at an electron dose of 3.0×10^4 $e^-/Å^2$. If the SNR of the spectra is further improved, *e.g.*, by using hybrid pixel direct detectors or by employing high-dose STEM conditions with a larger probe current or a longer dwell time, the detection limit may be further reduced as suggested by the black dashed arrow in Fig. 3(b). Multivariate statistical analysis techniques, such as principal component analysis or non-negative matrix factorization, also offer effective means for enhancing the SNR by extracting statistically significant signals [22, 23]. However, in this study, the slopes in the 3.6–4.6 eV range were obtained through linear fitting, a method inherently robust to noise, which limits the extent of potential SNR improvement. Thus, we conjecture that the detection limit could be lowered to approximately 0.1% at best.

Fig. 3

Structural analysis of He-ion implanted GaN

Elemental analysis

Structural analysis was conducted to verify that the shape modulation in the valence-loss spectra was induced by defects. First, we investigated whether He-ion implantation affected the elemental composition because the ADF image in Fig. 2(a) exhibits brighter contrast at a depth of approximately 100 nm, where the defect concentration is at its maximum. Figure 4(a) presents the depth profile of elemental composition. When the electron probe was incident along the GaN <11-20> zone-axis direction (tilt 0°), the composition deviated significantly from stoichiometry (Ga:N = 1:1), showing a higher Ga ratio. To further assess this phenomenon, an XEDS analysis was performed under a tilted condition, away from the zone-axis direction. Figure 4(b) displays the HAADF image indicating the XEDS measurement region and tilt direction. When the probe incidence direction was tilted approximately 10° parallel to the interface, the composition approached stoichiometry. One of the causes for the compositional deviation from stoichiometry even under the tilted condition may be the neglect of X-ray absorption effects in quantification. Although absolute composition values differ between the tilted and non-tilted conditions, the ratios remain consistent across all depths in both conditions, suggesting that He-ion implantation does not induce significant compositional modulation. The compositional uniformity is further corroborated by the HAADF image contrast in Fig. 4(b). Acquired at 300 kV, the HAADF image detects only electrons with large scattering vectors. Under these conditions, the HAADF image can be interpreted using the power-law model of Z-contrast [24], which suggests that the composition remains unchanged along the depth direction.

Fig. 4

To investigate the cause of the significant compositional deviation from stoichiometry under the zone-axis condition, electron propagation in the GaN wurtzite structure up to a thickness of 30 nm was simulated. Figure 4(c) presents the projected potential of GaN observed from the <11-20> direction. The simulation was conducted under two conditions, where the electron probes were positioned on Ga and N atomic columns as indicated by white circles. The corresponding simulated results are shown on the left and right sides of Fig. 4(d), respectively. In the case of the Ga atomic column, the intensity distribution of the electron probe remains localized near the atomic column at any thickness, with electrons primarily propagating along the atomic column in a phenomenon called channeling. Conversely, for the N atomic column, the intensity becomes delocalized and extends to the adjacent Ga atomic columns. The lower part of Fig. 4(d) shows the 2D intensity distribution at a thickness of 15 nm, revealing that the considerable intensity exists particularly in the first neighboring Ga atomic column. This phenomenon, known as dechanneling, results in the generation of more characteristic X-rays from Ga atoms under the zone-axis condition. Compositional deviation due to channeling in XEDS analysis has also been observed in other compound semiconductor systems [25], suggesting that channeling is the primary cause of the deviation from the stoichiometry of GaN. Because electron propagation is influenced by the crystal structure and orientation, the depth-independent composition ratio under both tilt conditions in Fig. 4(a) indicates that the GaN wurtzite structure remained essentially unchanged by He-ion implantation.

Disorder analysis via diffuse scattering

We further analyzed the scattering intensity distribution using 4D-STEM to investigate the origin of the brighter contrast at a depth of approximately 100 nm in the ADF image in Fig. 2(a). The ADF image was acquired at an acceleration voltage of 30 kV, where both electrons with large and small scattering vectors were detected. Under the condition, unlike the HAADF image in Fig. 4(b), additional contrast may arise due to the contribution of diffracted electrons [26]. Our previous study showed that scattering intensity distribution is useful for analyzing structural disorder and may provide insights into strain fields [11]. Figure 5(a) presents the virtual STEM image indicating the region of the 4D-STEM measurement, while representative convergent beam electron diffraction (CBED) patterns at different depths are shown in Fig. 5(b). Diffraction disks were observed in the GaN regions, and the patterns remained consistent regardless of the concentration of defects. This result indicates that there is no significant change in the GaN crystal structure or its orientation, aligning with the depth-independent composition observed with and without tilting in Fig. 4(a). Figure 5(c) presents the azimuthally averaged scattering intensity measured from each CBED pattern. The diffraction disk around 25 mrad was slightly broadened, and the low-angle scattering near the tail of the bright-field (BF) disk increased at depths with higher defect concentrations. Furthermore, high-angle diffuse scattering increased near the surface. Virtual STEM images reconstructed using scattering intensities in the ranges of 15–35 mrad (β_1) and 35–80 mrad (β_2) are presented in Fig. 5(d). The contrast in the virtual STEM images changed at a depth of approximately 100 nm, corresponding to the contrast modulation observed in the ADF image in Fig. 2(a). In X-ray analysis, it is well known that strain fields around defects generate diffuse scattering, such as Huang scattering or Stokes–Wilson scattering [27, 28]. Huang scattering near the diffraction peak reflects a long-range strain

field, while Stokes–Wilson scattering, which contributes to the background diffraction intensity, represents a short-range local strain field. Thus, Fig. 5(c) suggests that while the GaN crystal structure is preserved, a local strain field induced by defects exists at a depth of around 100 nm.

Fig. 5

Direct observation of crystal structures containing defect-induced local strain fields

Atomic resolution STEM images were acquired to directly observe crystal structures containing defect-induced local strain fields. Figure 6(a) shows low-magnification ABF images acquired at each depth. No extended defects, such as dislocations or stacking faults, were observed at any depth, whereas contrast modulation was clearly visible up to a depth of about 200 nm. Atomic resolution ABF and HAADF images are shown in Fig. 6(b), and the extracted HAADF intensity profiles across Ga atomic columns are shown in Fig. 6(c). In the contrast-modulated region at a depth of 100 nm in the HAADF image, the intensity decreased at atomic column positions and increased at intercolumn positions. Figure 6(d) represents one-dimensional intensity profiles obtained by azimuthally averaging fast Fourier transform (FFT) patterns of the HAADF images. The profile at a depth of 100 nm exhibits features similar to those in Fig. 5(c), with a slight broadening of the spots and an increase in the intensity of the low-frequency component. To visualize the low-frequency components, Fourier-filtered HAADF images were obtained by removing fundamental spots corresponding to the periodicity of the GaN crystal structure from the FFT patterns of the HAADF images, followed by inverse FFT. At a depth of 100 nm, an aperiodic component was observed in the area corresponding to the contrast modulation in the ABF image, while uniform contrast was confirmed at a depth of 500 nm.

These results demonstrate that some atoms are displaced from their original sites at a depth of 100 nm, indicating the existence of a local strain field.

Furthermore, we also prepared an ultrathin TEM sample with a thickness of approximately 10 nm for visualization of implantation-induced defects. Atomic-resolution ABF and HAADF images were acquired at a depth of 100 nm and are shown in Fig. 6(f). In the regions designated by the pink dashed circles, clear intensity modulation in atomic columns was observed, indicating the existence of disordered regions with a size of 1–2 nm. A previous study using molecular dynamics simulations predicted atomic configurations of defects produced in GaN crystal lattice by collision cascades under Si or Mg ion implantation and reported that defect clusters were formed due to aggregation of various kinds of vacancies and interstitial atoms [29]. Assuming the formation of similar defect clusters under the ion implantation condition of this study, the observed contrast modulation can be reasonably explained. The lower part represents repair of the crystal lattice in the left disordered region induced by electron-beam irradiation. Because point defects can readily migrate due to energy transfer from incident electrons, we infer that electron-beam irradiation induces migration of Frenkel pairs and the subsequent atomic rearrangement. The crystal lattice in the right disordered region did not repair due to the randomness of knock-on displacements. These observational results provide supporting evidence that the shape modulation in valence-loss spectra is caused by defects and defect-induced strain.

Fig. 6

We speculate that the detection limit of STEM observation is comparable to that of valence EELS because defect-induced contrast is observed at a depth of around 200 nm. However, because STEM observation using localized probes has a smaller interaction volume, its physical detection limit is likely higher than that of valence EELS. Assuming a defect concentration of 0.35% with defects uniformly and randomly distributed in a TEM sample of 50 nm thickness, the number of defects per unit area and per atomic column is estimated to be 15.4 defects/nm^2 and 0.48 defects/column, respectively. Because the number of defects per atomic column is less than 1, accurately evaluating the detection limit of STEM observation using this sample is challenging.

Relationship between shape modulation in valence-loss spectra and defects

A detailed structural analysis suggests the existence of local strain fields caused by defects at depths with higher defect concentrations. Atoms near these strain fields are displaced from their equilibrium positions. Consequently, GaN with a higher concentration of defects is expected to exhibit a crystal structure with larger atomic displacement parameters or an increased Debye–Waller factor, leading to an enhanced diffuse scattering as observed in Fig. 5. Note that the increase in sample temperature owing to electron irradiation is negligible because the interval of electron irradiation is on the order of nanoseconds for a probe current in the picoampere range, which is significantly longer than the phonon relaxation time, typically on the order of picoseconds or less. Previous studies have reported that strain alters the band structures of group-III nitrides nonlinearly and causes transition energy shifts [30, 31]. Based on this, we believe that the shift of the inflection points in Fig. 2(d) is attributed to defect-induced strain. Furthermore, the change in the bonding states of atoms around the defects, along with the

surrounding strain fields, likely contributes to the decrease in slopes at 3.6–4.6 eV. Because no clear mid-gap states were observed below 3.4 eV in Fig. 2, we believe that the surrounding strain fields play a significant role in this shape modulation of the valence-loss spectra.

Concluding remarks

In this study, we prepared GaN samples with controlled defect concentrations and investigated the detection limit of defects using valence EELS. By utilizing an appropriate TEM sample with a low physical limit, we determined the detection limit to be 0.35% (3500 ppm) under typical STEM conditions. A detailed structural analysis revealed the existence of defects and defect-induced strain, providing evidence that valence EELS can indirectly detect defects via local strain fields. The evaluated detection limit specifically corresponds to the detection limit of defect-induced strain, which was converted into point defect concentration. Because defects and strain are closely interrelated, this study offers valuable insights into the applicability of valence EELS for nanoscale defect detection. While the explanation of the causal relationship between the shape modulation in valence-loss spectra and defects remains incomplete, the integration of first-principles calculations may lead to a deeper understanding of this correlation.

References

[1] Crewe A V, Wall J, and Langmore J (1970) Visibility of Single Atoms. *Science* 168**:** 1338–1340. https://doi.org/10.1126/science.168.3937.1338.

[2] Smith B W, Monthioux M, and Luzzi D E (1998) Encapsulated C60 in Carbon Nanotubes. *Nature* 396: 323–324. https://doi.org/10.1038/24521.

[3] Suenaga K, Tencé M, Mory C, Colliex C, Kato H, Okazaki T, Shinohara H, Hirahara K, Bandow S, and Iijima S (2000) Element-Selective Single Atom Imaging. *Science* 290: 2280–2282. https://doi.org/10.1126/science.290.5500.2280.

[4] Hashimoto A, Suenaga K, Gloter A, Urita K, and Iijima S (2004) Direct Evidence for Atomic Defects in Graphene Layers. *Nature* 430: 870–873. https://doi.org/10.1038/nature02817.

[5] Krivanek O L, Chisholm M F, Nicolosi V, Pennycook T J, Corbin G J, Dellby N, Murfitt M F, Own C S, Szilagyi Z S, Oxley M P, Pantelides S T, and Pennycook S J (2010) Atom-by-Atom Structural and Chemical Analysis by Annular Dark-Field Electron Microscopy. *Nature* 464: 571–574. https://doi.org/10.1038/nature08879.

[6] Suenaga K, and Koshino M (2010) Atom-by-Atom Spectroscopy at Graphene Edge. *Nature* 468**:** 1088–1090. https://doi.org/10.1038/nature09664.

[7] International Union of Pure and Applied Chemistry (IUPAC) (2019) Limit of detection. In: *Compendium of Chemical Terminology*, 4th ed. (the "Gold Book"). https://doi.org/10.1351/goldbook.L03540.

[8] Bowman W J, March K, Hernandez C A, and Crozier P A (2016) Measuring Bandgap States in Individual Non-Stoichiometric Oxide Nanoparticles Using Monochromated STEM EELS: The Praseodymium–Ceria Case. *Ultramicroscopy* 167: 5–10. https://doi.org/10.1016/j.ultramic.2016.04.009.

[9] Wang S, March K, Ponce F A, and Rez P (2019) Identification of Point Defects Using High-Resolution Electron Energy Loss Spectroscopy. *Phys. Rev. B* 99: 115312. https://doi.org/10.1103/PhysRevB.99.115312.

[10] Asano T, Tezura M, Saitoh M, Tanaka H, Kikkawa J, and Kimoto K (2022) Nanoscale Observation of Subgap Excitations in β-Si_3N_4 with a High Refractive Index Using Low-Voltage Monochromated STEM: A New Approach to Analyze the Physical Properties of Defects in Dielectric Materials. *Appl. Phys. Express* 15: 076501. https://doi.org/10.35848/1882-0786/ac6e28.

[11] Yamashita S, Fukushima S, Kikkawa J, Arai R, Kanitani, Y, Kimoto K, and Kudo Y (2024) Local Defect and Mid-Gap State Analysis of GaN Using Monochromated EELS Combined with Nanodiffraction and Atomic-Resolution Imaging. *APL Mater.* 12: 031101. https://doi.org/10.1063/5.0178995.

[12] Ziegler J F, Ziegler M D, and Biersack J P (2010) SRIM – The Stopping and Range of Ions in Matter (2010). *Nucl. Instrum. Methods Phys. Res. B: Beam Interact. Mater. At.* 268: 1818–1823. https://doi.org/10.1016/j.nimb.2010.02.091.

[13] Ebata S, Ishihara M, Uchino K, Itose S, Matsuya M, Kudo M, Bajo K, and Yurimoto H (2012) Development of Laser Ionization Mass Nanoscope (LIMAS). *Surf. Interface Anal.* 44: 635–640. https://doi.org/10.1002/sia.4857.

[14] Egerton R F (2017) Scattering Delocalization and Radiation Damage in STEM-EELS. *Ultramicroscopy* 180: 115–124. https://doi.org/10.1016/j.ultramic.2017.02.007.

[15] Malis T, Cheng S C, and Egerton R F (1998) EELS Log-Ratio Technique for Specimen-Thickness Measurement in the TEM. *J. Elec. Microsc. Tech.* 8: 193–200. https://doi.org/10.1002/jemt.1060080206.

[16] Iakoubovskii K, Mitsuishi K, Nakayama Y, and Furuya K (2008) Thickness measurements with electron energy loss spectroscopy. *Microsc. Res. Tech.* 71: 626–631. https://doi.org/10.1002/jemt.20597.

[17] Gu L, Srot V, Sigle W, Koch C, van Aken P, Scholz F, Thapa S B, Kirchner C, Jetter M, and Rühle M (2007) Band-Gap Measurements of Direct and Indirect Semiconductors Using Monochromated Electrons. *Phys. Rev. B* 75: 195214. https://doi.org/10.1103/PhysRevB.75.195214.

[18] Madsen J, and Susi T (2021) The abTEM code: transmission electron microscopy from first principles. *Open Res. Europe* 1: 24. https://doi.org/ 10.12688/openreseurope.13015.1

[19] Pennycook S J, and Jesson D E (1999) High-Resolution Z-Contrast Imaging of Crystals. *Ultramicroscopy* 37: 14–38. https://doi.org/10.1016/0304-3991(91)90004-P.

[20] Findlay S D, Shibata N, Sawada H, Okunishi E, Kondo Y, and Ikuhara Y (2010) Dynamics of Annular Bright Field Imaging in Scanning Transmission Electron Microscopy. *Ultramicroscopy* 110: 903–923. https://doi.org/10.1016/j.ultramic.2010.04.004.

[21] Yamashita S, Koshiya S, Nagai T, Kikkawa J, Ishizuka K, and Kimoto K (2015) Quantitative Annular Dark-Field Imaging of Single-Layer Graphene—II: Atomic-Resolution Image Contrast. *Microscopy* 64: 409–418. https://doi.org/10.1093/jmicro/dfv053.

[22] Shiga M, Tatsumi K, Muto S, Tsuda K, Yamamoto Y, Mori T, and Tanji T (2016) Sparse modeling of EELS and EDX spectral imaging data by nonnegative matrix factorization. *Ultramicroscopy* 170: 43–59. https://doi.org/10.1016/j.ultramic.2016.08.006.

[23] Yamashita S, Tanabe M, Araki T, Shiomi M, Nishi T, and Kudo Y (2022) Nanostructure–Optical Property Relationship in $CuInSe_2$/ZnS Core/Shell Quantum Dots Revealed by Multivariate Statistical Analysis of X-ray Spectrum Images. *J. Phys. Chem. C* 126: 14558–14565. https://doi.org/10.1021/acs.jpcc.2c03619.

[24] Yamashita S, Kikkawa J, Yanagisawa K, Nagai T, Ishizuka K, and Kimoto K (2018) Atomic Number Dependence of Z Contrast in Scanning Transmission Electron Microscopy. *Sci. Rep.* 8: 12325. https://doi.org/10.1038/s41598-018-30941-5.

[25] Ek M, Lehmann S, and Wallenberg R (2020) Electron channelling: challenges and opportunities for compositional analysis of nanowires by TEM. *Nanotechnology* 31: 364005. https://doi.org/10.1088/1361-6528/ab9679

[26] Yu Z, Muller D A, and Silcox J (2004) Study of Strain Fields at a-Si/c-Si Interface. *J. Appl. Phys.* 95: 3362–3371. https://doi.org/10.1063/1.1649463.

[27] Dederichs P H (1973) The Theory of Diffuse X-Ray Scattering and Its Application to the Study of Point Defects and Their Clusters. *J. Phys. F: Met. Phys.* 3: 471–496. https://doi.org/10.1088/0305-4608/3/2/010.

[28] Haubold H-G (1976) Application of X-Ray Diffuse Scattering to Structure Determinations of Point-Defects. *Rev. Phys. Appl. (Paris)* 11: 73–81. https://doi.org/10.1051/rphysap:0197600110107300.

[29] Kamiński P, Turos A, Kozłowski R, Stefańska-Skrobas K, Żelazko J, and Grzanka E (2024) Deep-level defects induced by implantations of Si and Mg ions into undoped epitaxial GaN. *Sci. Rep.* 14: 14272. https://doi.org/10.1038/s41598-024-65142-w.

[30] Benaissa M, Sigle W, Zaari H, Tadout M, and van Aken P A (2017) Strain and size combined effects on the GaN band structure: VEELS and DFT study. *Phys. Chem. Chem. Phys.* 19: 5430–5434. https://doi.org/10.1039/C6CP08642J.

[31] Yan Q, Rinke P, Janotti A, Scheffler M, and Van de Walle C G (2014) Effects of strain on the band structure of group-III nitrides. *Phys. Rev. B* 90: 125118. https://doi.org/10.1103/PhysRevB.90.125118.

Figure Legends

Fig. 1 Details of He-ion implanted GaN. (a) Schematic illustration of the three-step He-ion implantation process. (b) Experimental and simulated depth profiles of He-ion concentration. Filled markers and open markers represent experimental results measured by SIMS and simulated results obtained using the SRIM, respectively. (c) Depth profile of defect concentration simulated by the SRIM. (d) Relationship between the physical limit and TEM sample thickness of GaN for valence EELS measurements. The analytical area for each probe position is assumed to be 16 nm^2 for an acceleration voltage of 30 kV and energy losses of approximately 3–5 eV.

Fig. 2 Depth-dependent valence-loss spectra of He-ion implanted GaN. (a) ADF image acquired simultaneously with EEL spectrum imaging data. (b) Valence-loss spectra collected from the surface to a depth of 1600 nm. Each spectrum was obtained by integrating 18 spectra at each depth, with an electron dose of 5.4×10^5 $e^-/Å^2$. (c) Smoothed spectra from the surface to a depth of 600 nm processed using a Savitzky–Golay filter. The red arrow indicates the inflection points at the onsets, while the red lines indicate the slopes at 3.6–4.6 eV, determined via linear fitting. (d) Depth dependence of the inflection points. (e) Depth dependence of the slopes in the 3.6–4.6 eV range. The standard deviations σ in (d) and (e) were calculated by linear approximation for all data points below a depth of 600 nm. The shaded areas in (d) and (e) represent three standard deviations (±3σ) from the dashed grey lines corresponding to the approximated lines.

Fig. 3 Relationship between electron dose and detection limit. (a) Effect of electron dose on the depth dependence of the slopes in the 3.6–4.6 eV range. The corresponding electron doses are indicated at the top. The red arrows indicate the maximum depth at which the slope exhibited

significant changes beyond the ±3σ region. (b) Evaluated detection limit at each electron dose, determined from the maximum depth shown in (a). The grey line represents the defect concentration depth profile simulated using the SRIM, as shown in Fig. 1(c).

Fig. 4 Elemental analysis by STEM-XEDS. (a) Depth profile of elemental composition. Closed circles represent measurement values without tilt (orange for Ga; blue for N), while open circles represent the measurement values with tilt (red for Ga; green for N). (b) HAADF image indicating the XEDS measurement region, with the black arrow showing the tilt direction. (c) Projected potential of GaN observed from the <11-20> zone-axis direction. (d) Simulated intensity distributions of incident electron probes positioned at Ga (left) and N (right) atomic columns. The upper and lower panels illustrate electron propagation in 3D and 2D representations, respectively. The lower panels show intensity distribution at a thickness of 15 nm.

Fig. 5 Disorder analysis via diffuse scattering. (a) Virtual STEM image showing the region of the 4D-STEM measurement. (b) Representative CBED patterns of the He-ion implanted GaN at depths of 100, 200, and 500 nm. A CBED pattern of the amorphous carbon (a-Carbon) protective layer is also included as a reference. (c) Azimuthally averaged scattering intensities extracted from each CBED pattern, with diffraction peak positions of GaN shown for comparison. (d) Virtual STEM images reconstructed using diffraction intensities within the ranges indicated by β_1 and β_2 in (c).

Fig. 6 Atomic structures of He-ion implanted GaN. (a) Low-magnification ABF images showing contrast modulation below a depth of 200 nm. (b) Atomic-resolution ABF and HAADF images. (c) HAADF intensity profiles across Ga atomic columns along the lines marked by triangles in

(b). (d) Azimuthally averaged radial intensity profiles of FFT patterns from each HAADF image, with GaN diffraction peaks from Fig. 5(c) included for comparison. (e) Fourier-filtered HAADF images highlighting the local strain field at a depth of 100 nm. (f) Atomic-resolution ABF and HAADF images acquired at a depth of 100 nm using the ultrathin TEM sample. Pink dashed circles indicate the disordered regions containing defect clusters. The lower part represents the disappearance of the defect cluster, *i.e.*, the repair of the GaN crystal lattice, probably due to the migration of Frenkel pairs induced by electron-beam irradiation.

Mini Abstract

We investigated the detection limit of defect-induced strain in GaN using valence EELS and correlated structural analysis. The detection limit fundamentally depends on the signal-to-noise ratio of the valence-loss spectra and was determined to be 0.35% (3500 ppm) under a typical STEM electron dose condition.

Mini Abstract Figure: Figure 2 and 3

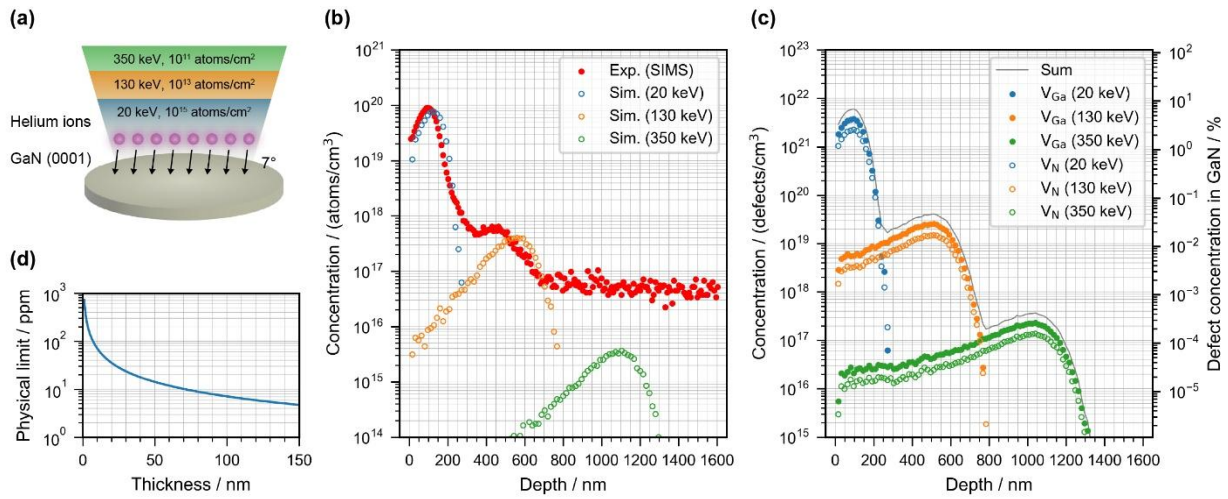

Figure 1

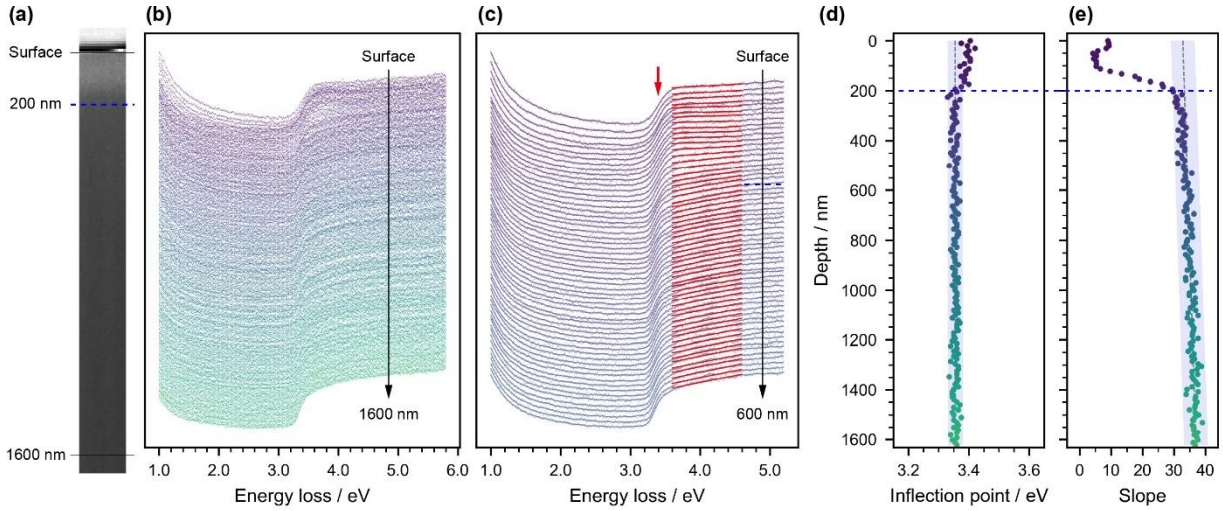

Figure 2

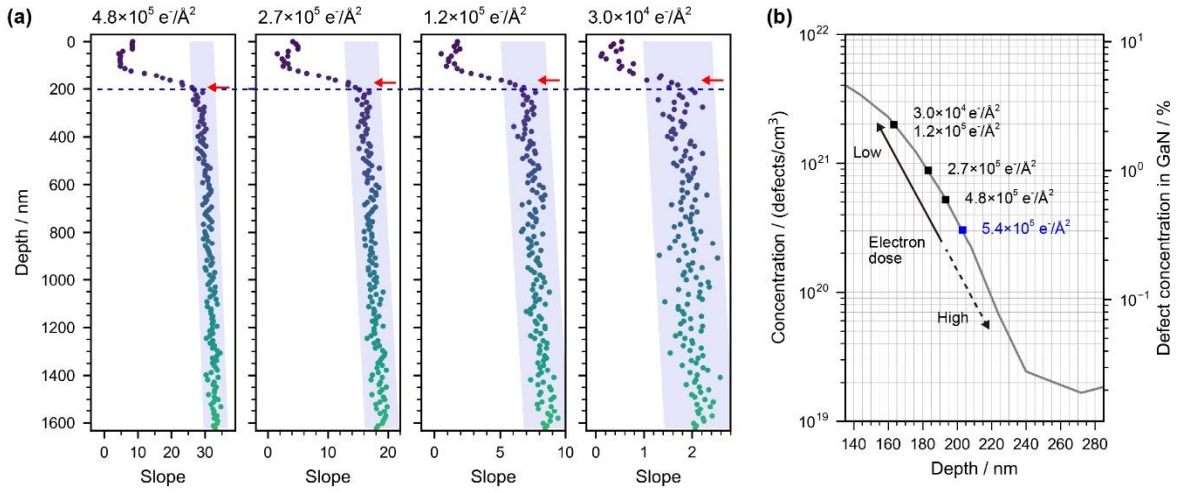

Figure 3

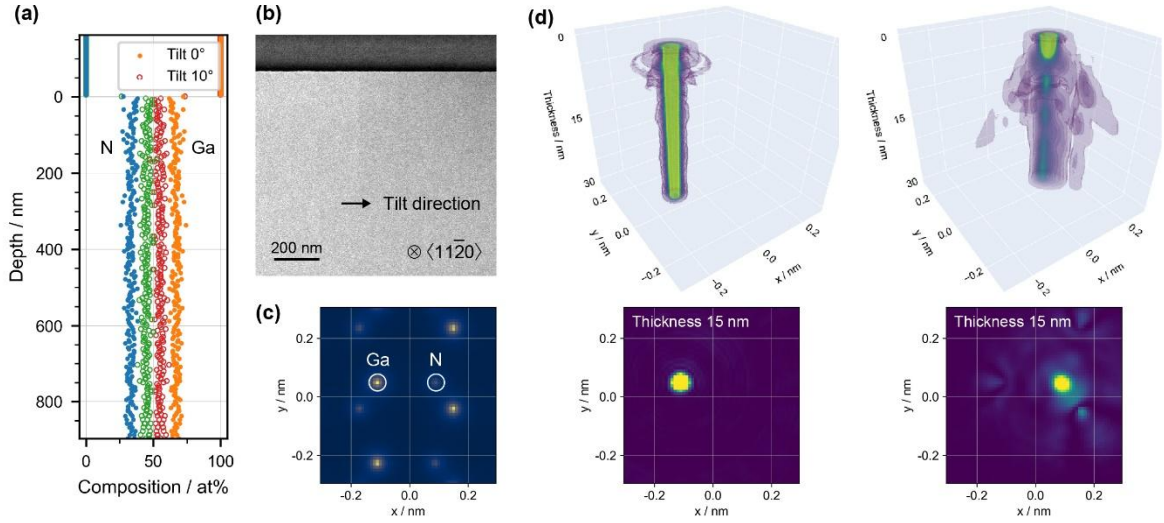

Figure 4

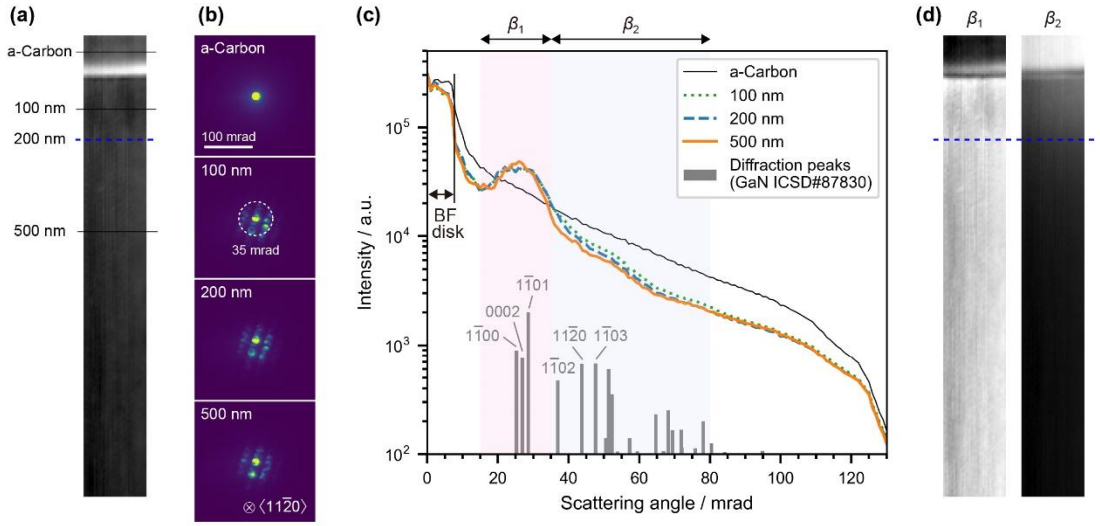
(a)
a-Carbon
100 nm
200 nm
500 nm
(b)
a-Carbon
100 mrad
100 nm
35 mrad
200 nm
500 nm
⊗⟨11$\bar{2}$0⟩
(c)
β_1
β_2
a-Carbon
100 nm
200 nm
500 nm
Diffraction peaks
(GaN ICSD#87830)
BF
disk
Intensity / a.u.
10^5
10^4
10^3
10^2
$1\bar{1}01$
0002
$1\bar{1}00$
$11\bar{2}0$
$1\bar{1}03$
$1\bar{1}02$
0
20
40
60
80
100
120
Scattering angle / mrad
(d)
β_1
β_2

Figure 5

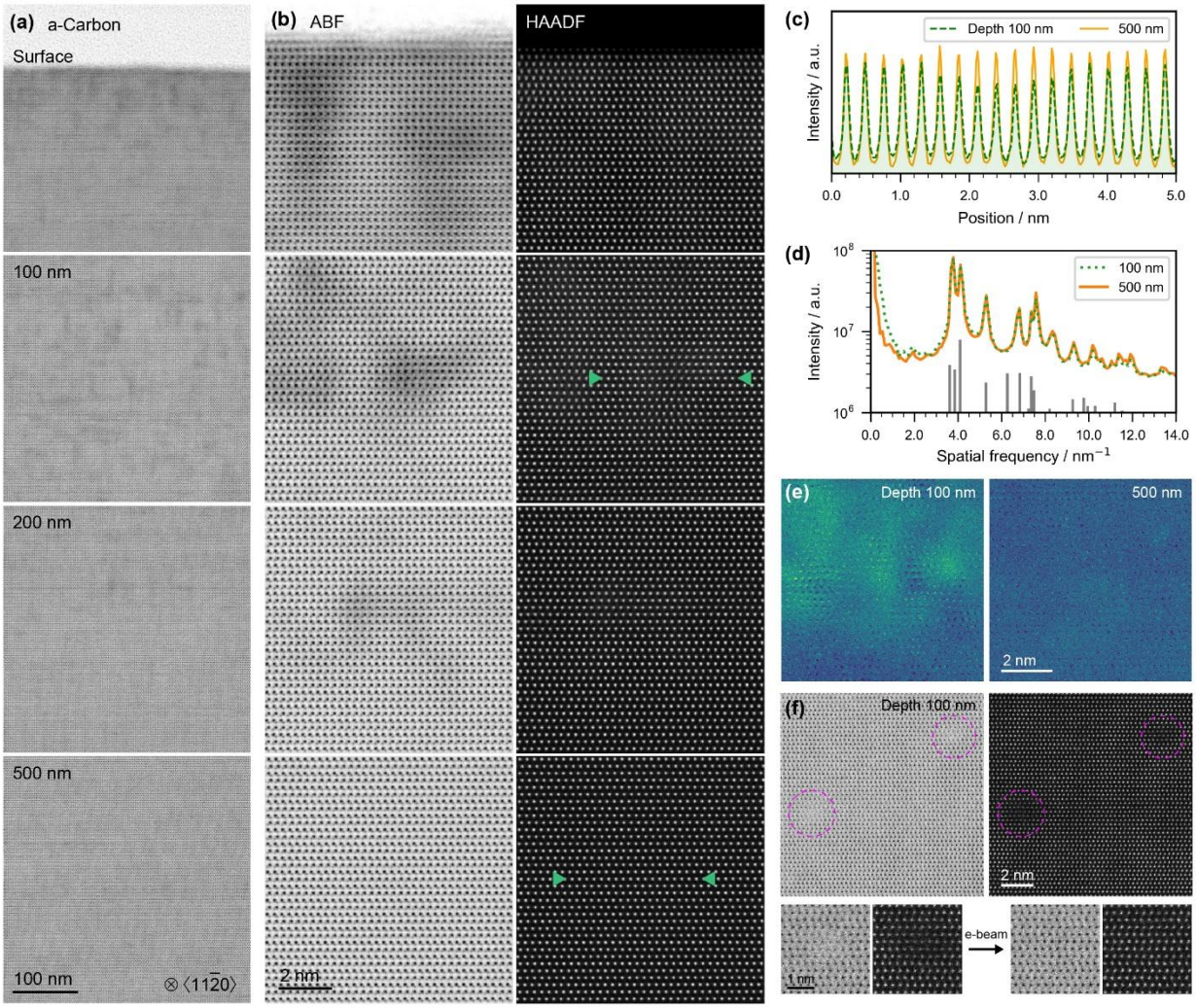
(a) a-Carbon
Surface
100 nm
200 nm
500 nm
100 nm
⊗ ⟨11$\bar{2}$0⟩
(b) ABF
HAADF
2 nm
(c)
Depth 100 nm
500 nm
Intensity / a.u.
Position / nm
(d)
100 nm
500 nm
Intensity / a.u.
Spatial frequency / nm^{-1}
(e)
Depth 100 nm
500 nm
2 nm
(f)
Depth 100 nm
2 nm
e-beam
1 nm

Figure 6